Optical characterization of Pr^{3+}-doped yttria-stabilized zirconia single crystals

B. Savoini, J. E. Muñoz Santiuste, and R. González
Departamento de Física, Escuela Politécnica Superior, Universidad Carlos III de Madrid, Butarque 15, Leganés E-28913, Madrid, Spain
(Received 7 March 1997)

The optical absorption and fluorescence of Pr^{3+} ions in yttria-stabilized zirconia single crystals are investigated. Fluorescence emissions from the $^1D_2$ level are clearly dominant and low intensity emission lines from the $^3P_0$ and $^1G_4$ states are also observed. Analysis with the Judd-Ofelt theory of the absorption intensities has been made assuming that only ~40% of the praseodymium ions contribute to the optical absorption bands. Quantum efficiency values of $\eta(^3P_0)\sim 0.2$ and $\eta(^1D_2)\sim 1$ are obtained at room temperature. $^1D_2$ fluorescence quenching has been observed in heavily-doped samples due to cross relaxation processes among neighboring Pr^{3+} ions. Analysis using the Inokuti-Hirayama model shows that electric dipole-dipole interactions are mainly responsible for the quenching effect. Pr^{3+} ions are present in seven and sixfold configurations with a statistical distribution. The energy position of the $4f5d$ configuration is very different for each center. The fluorescence dynamics is explained by a mechanism involving thermally assisted population of the $^3P_{1,2}+^1I_6$ upper levels and fast relaxation to the $^1D_2$ level via states of the excited $4f5d$ configuration. [S0163-1829(97)02734-3]

I. INTRODUCTION

The fluorescence of Pr^{3+} ions has been intensively studied in the last decades in a large variety of crystalline and glass materials. Interest in studying Pr^{3+}-doped solid-state materials has been renewed due to the fact that its emission spectra have been extended from the blue to the near infrared region.[1] Laser action has been reported for Pr^{3+} ions in different crystals such as YAG, $LiYF_4$, and $YAlO_3$ as well as in fibers.[1–4] Additionally, up-conversion lasing under IR excitation has been demonstrated in Pr^{3+}-doped systems;[5] this is important in developing compact systems using IR laser diode pumping devices. The Pr^{3+} luminescence mainly originates at transitions from $^3P_0$ or $^1D_2$ multiplets of the $4f^2$ configuration of the Pr^{3+} ion. Other important transitions for laser applications start from the $^1G_4$ state.[6]

Yttria-stabilized zirconia (YSZ) is a solid ionic conductor with applications ranging from oxygen sensors to solid fuel cells.[7] Its high ionic conductivity at high temperatures is related to oxygen vacancies already present in the YSZ crystal associated with the charge compensation induced when Y_2O_3 is added to ZrO_2 to stabilize the cubic phase. The vacancy site has been intensively investigated in recent years.[8–10] The possibility of growing large YSZ crystals of good optical quality makes this system a good candidate to be used in optical devices. Laser action has been reported for Nd^{3+}-doped YSZ and yttria-stabilized hafnia (YSHf) and for erbia-stabilized zirconia (ErSZ) doped with several rare-earth ions (Ho^{3+}, Tm^{3+}, or Er^{3+}).[1,2]

YSZ or $(ZrO_2)_{1-x}(Y_2O_3)_x$ has the CaF_2 structure for a wide range of x values. The sites of impurity ions and their associated oxygen vacancy redistribution have been analyzed using luminescence as an optical probe.[8,11–14] Because of the highly distorted structure, impurities can be located in a large number of sites. This inherent disorder is responsible for inhomogeneously broad optical bands even at very low temperatures. Oxygen vacancies result in slight departures of the local environment from the fluorite-type lattice. The oxygen coordination around active impurities is not only eightfold (CN8) but also sevenfold (CN7) and sixfold (CN6).[14] CN6, CN7, and CN8 environments have been reported for Eu^{3+} and Er^{3+}-doped YSZ,[11,12,14] with the amount of ions in each site strongly depending on the crystal composition. However, some impurities such as Nd^{3+} are incorporated only in CN7 configurations.[13] Impurity ions are located at cation sites; the ideal site symmetry is O_h for ions in CN8 sites, C_{3v} symmetry for ions in CN7 sites, and C_{3i}/S_6 or C_2 in CN6 sites.

Praseodymium ions may adopt both 3+ and 4+ states. Formation of oxygen-deficient praseodymium compounds Pr_6O_{11} ($4\ PrO_2 + Pr_2O_3$) and Pr_7O_{12} ($3\ PrO_2 + 2\ Pr_2O_3$) with the fluorite like structure,[15] where only 1/3 and 4/7 of the praseodymium ions, respectively, are in the trivalent state, is well known. In YSZ praseodymium ions can substitute Y^{3+} and Zr^{4+} cations and appear in both valence states. Pr^{3+} to Pr^{4+} conversion has been observed in the Pr_2O_3-ZrO_2 solid solution, making it unsuitable as a solid-state electrolyte.[16]

In this paper, an extensive investigation of the optical properties (absorption and luminescence) of Pr^{3+}-doped YSZ crystal is reported. We have studied the luminescence decay curves of the $^3P_0$ and $^1D_2$ levels which are mainly responsible for the luminescence. From these data, the fluorescence dynamics has been analyzed. Under the assumption that only a fraction of praseodymium ions contribute to their luminescence properties, the Judd-Ofelt theory is successfully used to estimate the quantum efficiency of the main luminescence channels. Concentration effects have also been investigated.

II. EXPERIMENTAL PROCEDURE

Single crystals of ZrO_2 stabilized with 16 wt % of Y_2O_3 and doped with 0.05 and 0.2 wt % of Pr_2O_3 were

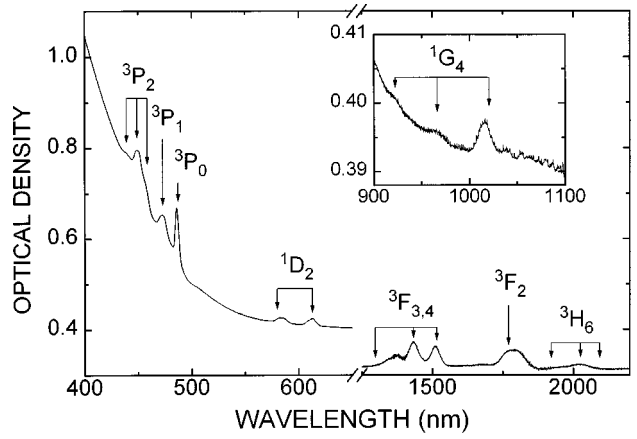

FIG. 1. Room-temperature absorption spectrum of a Pr^{3+}-doped YSZ crystal. The inset shows an enlargement of the $^3H_4 \rightarrow {}^1G_4$ transition. Final levels involved in the transitions are indicated.

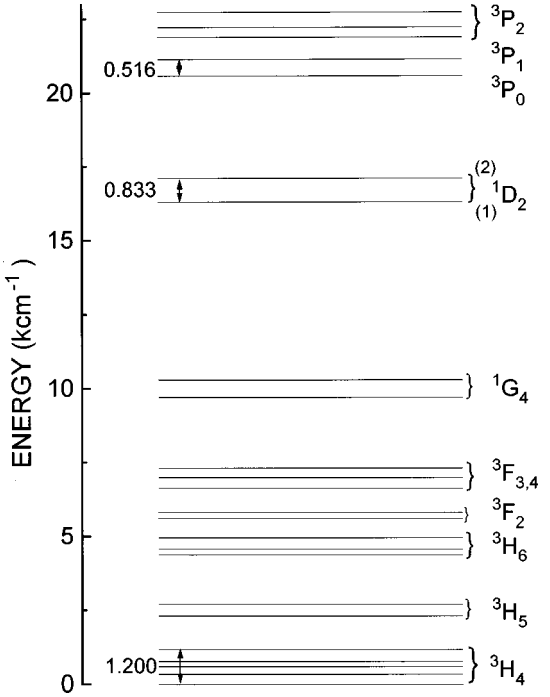

FIG. 2. Energy level diagram of Pr^{3+}-doped YSZ crystals.

purchased from CERES Corporation. Excellent optical quality crystals were grown by the skull method. The sample density is 5.9 g/cm^3 and the refractive index is about 2.17 at 500 nm.

Samples were cut with a diamond saw and polished to optical quality. X-ray fluorescence analysis of two types of as-received crystals show that their compositions are $Y_{0.193}Hf_{0.085}Zr_{0.795}Pr_{0.010}O_{1.901}$ and $Y_{0.190}Hf_{0.082}Zr_{0.794}Pr_{0.072}O_{1.901}$ which implies praseodymium concentrations of 2.2×10^{19} cm^{-3} and 1.7×10^{20} cm^{-3}, respectively. Unless otherwise stated, the optical measurements were made in the former crystals.

Optical absorption measurements in the UV-visible-IR were made with a Perkin-Elmer Lambda 19. Infrared-absorption data were taken with a Perkin-Elmer 2000 Fourier-transform IR spectrometer. Both excitation and fluorescence measurements were made with either a Jobin-Yvon or a Perkin-Elmer spectrofluorimeter. For high-resolution emission measurements a Spectra Physics Ar^+ laser was used as the excitation source. The emitted light was focused into the entrance slit of a SPEX 1000M monochromator and detected with either a Hamamatsu R943-02 cooled photomultiplier or a InGaAs Hamamatsu G3476-03 photodiode. The spectra were recorded with a SR400 gated photon counter or a HP 7240 nanovoltmeter. For lifetime measurements a Spectra Physics MOPO 730-10 was used as the pulsed excitation source. The fluorescence decay was recorded in a Tektronix 2440 digital oscilloscope. Low-temperature measurements were made with either an optical He closed-cycle Leybold cryostat or a liquid-helium evaporation Oxford cryostat.

Thermal anneals in a reducing atmosphere were performed with the samples inside a graphite container surrounded by flowing nitrogen gas inserted in a horizontal furnace. High-temperature oxidizing treatments were made in flowing oxygen gas.

III. RESULTS AND DISCUSSION

A. Absorption spectra

Figure 1 shows the room-temperature (RT) absorption spectrum of a YSZ:Pr^{3+} crystal in the 400–2200 nm interval. Four groups of broad absorption bands, corresponding to transitions between the $^3H_4$ ground state and excited states inside the $4f^2$ configuration of the Pr^{3+} ion, are observed. The structure of each band is due to the stark splitting of the different multiplets by the matrix crystal field. Due to the highly distorted structure of YSZ, absorption lines have a large inhomogeneous broadened half-width, and no individual centers can be identified. The absorption transitions have been assigned by comparing our absorption spectrum with previous data.[1,17,18] The high-energy group overlaps with the absorption edge of the matrix at about 450 nm and was associated with transitions from the $^3H_4$ state to the $^3P_{0,1,2}+{}^1I_6$ multiplets. The two broadbands located at about 600 nm were associated with transitions from the $^3H_4$ ground state to the two Stark components of the $^1D_2$ state. The strong splitting ($\sim$ 800 cm^{-1}) observed in this transition indicates a relatively intense crystal field around the Pr^{3+} ion. The inset shows the weak bands centered at about 1000 nm which correspond to the spin forbidden $^3H_4 \rightarrow {}^1G_4$ transitions. The near-infrared groups (1200–2200 nm) were associated with transitions to the $^3F_{2,3,4}$ multiplet and $^3H_6$ states. It should also be noted that the absorption lines located at $\sim$ 4000 nm (not shown in the figure) corresponding to $^3H_4 \rightarrow {}^3H_5$ transitions were not clearly resolved due both to their low intensities and to the fact that they strongly overlap with the CO_2 lines always present in the atmosphere.

Figure 2 depicts the energy diagram of the Pr^{3+} ion derived from the absorption spectrum. The position of the $^3H_5$ band inferred from the emission spectra is also included. In this scheme the $^1S_0$ and $^1I_6$ states are absent. The former lies at very high energies ($\sim$ 46 000 cm^{-1} is usually accepted) from the ground state; the latter is not observed in

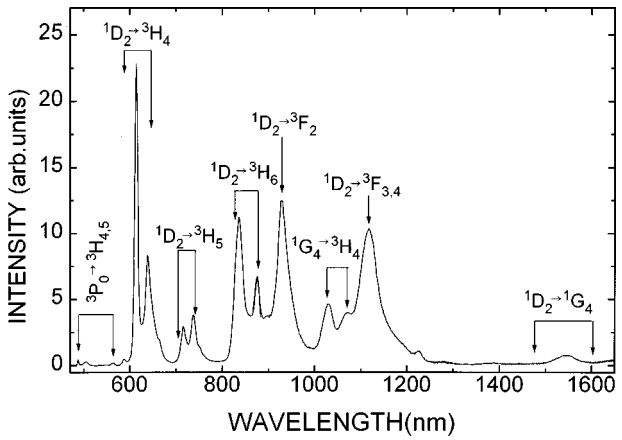

FIG. 3. Room-temperature emission spectrum for a YSZ:Pr^{3+} crystal (λ_{ex}= 457 nm). Levels involved in the transitions are indicated. The intensities are corrected for detector response.

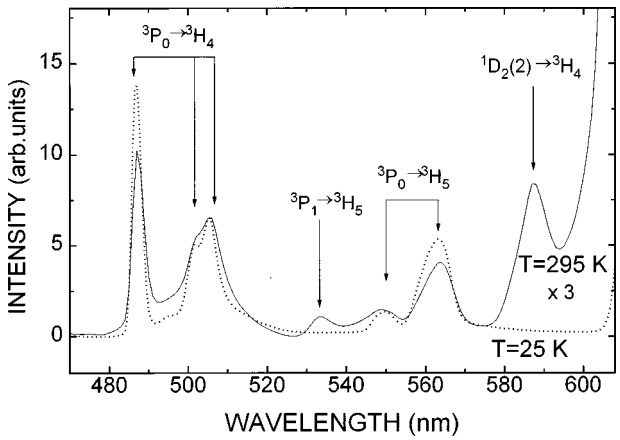

FIG. 4. Emission spectra at 295 K and 25 K for a YSZ:Pr^{3+} crystal (λ_{ex}=457 nm). The RT spectrum is enlarged 3 times. The intensities are corrected for detector response.

the absorption spectra due to the spin-forbidden character of the $^3H_4 \rightarrow {}^1I_6$ transition and is assumed to be close in energy to the $^3P_1$ state.[18]

By analogy with the absorption bands of the isoelectronic Ce^{3+} ion, the $f \rightarrow d$ absorption bands of Pr^{4+} ions are expected to occur in the 300–400 nm region.[18] A previous work assigned the low energy side of the absorption edge to a broad absorption band related to Pr^{4+} ions.[17] This band disappears after annealing in vacuum at $\sim$1173 K. It is well known that a broad absorption band peaking at 375 nm is also present in undoped YSZ crystals, making the previous assignment of this band to Pr^{4+} very doubtful.[19–21] In addition, thermal anneals up to 1900 K in oxidizing or reducing atmospheres do not change the absorption intensities of the Pr^{3+} absorption lines, indicating that valence state conversion $3+ \leftrightarrow 4+$ did not occur and that both Pr^{3+} and Pr^{4+} ions are very stable. In conclusion, the absorption band at the absorption edge cannot be definitely assigned to Pr^{4+} ions.

B. Fluorescence experiments

Figure 3 shows the emission spectra obtained under excitation in the $^3P_2$ multiplet (457 nm). The high intensity lines correspond to transitions from the $^1D_2$ level. The $^1D_2 \rightarrow {}^1H_4$ emission transition (615 and 641 nm lines) was clearly dominant and produced a relatively intense red-orange luminescence. Emissions from the $^3P_0$ state were of low intensity compared with the aforementioned ones and were better resolved at low temperatures. Some of the emission lines present in the spectrum shown in Fig. 3 were absent when the crystal was excited in the $^1D_2$ region (585 nm), thus allowing separation of the transition lines starting from these levels from those which originate at the ^3P_J levels. Two luminescence spectra were recorded under excitation with two other argon laser lines (477 and 489 nm); small changes observed in the relative intensity of some luminescence peaks suggest that more than one type of center is present, as occurs in other rare-earth-doped YSZ.[11–13] Low-temperature emission spectra showed the same emission lines as in the RT spectra but with higher resolution due to thermal depopulation of the upper levels. A significant increase of the relative intensity of the transitions from the $^3P_0$ levels could be observed. Figure 4 shows the low-intensity luminescence in the 470–600 nm region. Two lines at 534 and 588.5 nm disappeared, indicating that they are associated with transitions starting at thermally populated levels. These lines are ascribed to transitions from the $^3P_1$ level to the low-energy level of the $^3H_5$ multiplet (534 nm) and from the highest-energy band of the $^1D_2$ multiplet to the ground state; we have labeled this 588.5 nm line as $^1D_2(2) \rightarrow {}^3H_4$ in Fig. 4.

The excitation spectra of YSZ:Pr^{3+} recorded for three emission wavelengths (505, 533, and 640 nm) are shown in Fig. 5. The appearance of the $^3P_{0,1,2}$ bands in the excitation spectra of the $^1D_2 \rightarrow {}^3H_4$ luminescence (640 nm) clearly indicates that a nonradiative relaxation from the $^3P_{0,1,2}$ levels to the $^1D_2$ state occurs. The luminescence originates primarily at this latter level. In addition, a broad and structured band could be observed in the near-ultraviolet region (200–350 nm). This band had two main peaks at 280 and 320 nm whose relative intensity changed with the emission wavelength. Excitation of this band produced the characteristic luminescence spectrum of the Pr^{3+} ion but the intensity of the transitions from the $^1D_2$ level increased relative to those

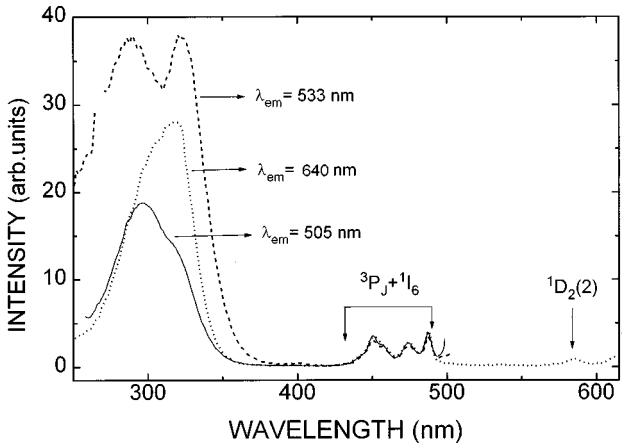

FIG. 5. RT excitation spectra of a YSZ:Pr^{3+} crystal for three emission wavelengths: λ_{em}=505 nm (solid line), λ_{em}=533 nm (dashed line), and λ_{em}=640 nm (dotted line). The spectra are normalized to the ^3P_J band intensities.

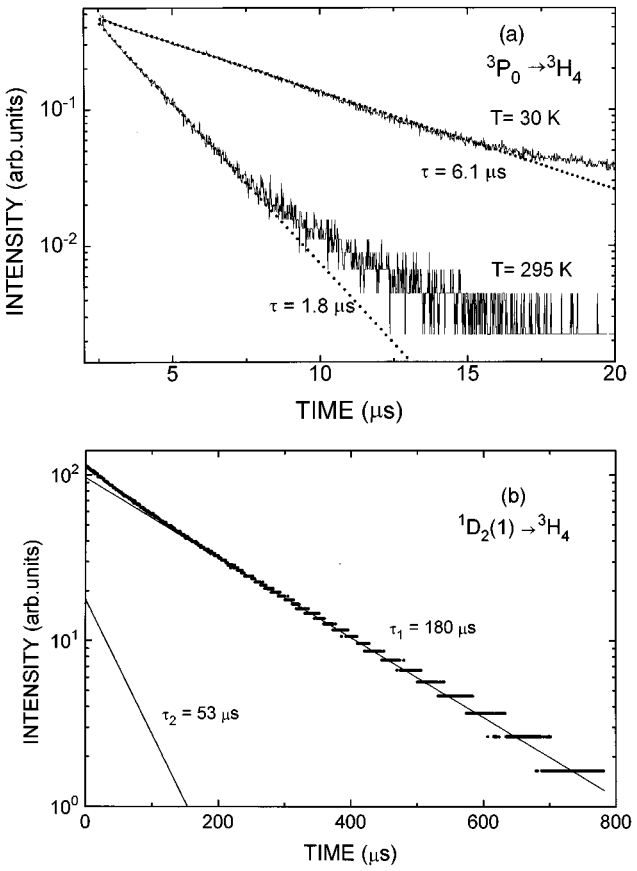

FIG. 6. Decay time curves of the (a) $^3P_0 \rightarrow ^3H_4$ luminescence at 295 and 30 K (λ_{ex}= 457 nm) and (b) $^1D_2(1) \rightarrow ^3H_4$ luminescence (λ_{ex}=488 nm). Decomposition on two exponential decays is showed.

starting at the $^3P_0$ levels. Intrinsic luminescence was also induced under UV excitation.[20] Based on previous assignments of the $4f^2 \rightarrow 4f5d$ excitation transition in Pr^{3+} ions,[21–25] we associate the excitation band at 320 nm with Pr^{3+} ions in CN7 sites, while the band peaking at 280 nm is related both with the Pr^{3+} ions in CN6 sites and with excitation of the intrinsic YSZ luminescence.

C. Lifetime measurements

Analysis of the luminescence decay curves provides information on the luminescence processes. Measurements of the luminescence decays from both the $^3P_0$ and $^1D_2$ levels were carried out at temperatures from 15 to 300 K.

Figure 6(a) shows the luminescence decays from the $^3P_0$ level. Nearly exponential decays were observed, with lifetimes changing from 6.1 to 1.8 μs as the temperature increases. The slow component of the decay curve is better resolved at low temperature and is mainly related to the intrinsic luminescence, always present in the sample, which has a much longer lifetime.[26] Decay curves from the $^1D_2$ level are nonexponential and are decomposed in two exponential decays, with τ_1=180 μs and τ_2=53 μs, being $\approx$82% and $\approx$18% the percentages of the initial intensity of each lifetime component, τ_1 and τ_2, respectively [see Fig. 6(b)]. These decays are temperature independent. The nonexponential behavior can be associated with either some kind of nonradiative losses or Pr^{3+} ions in different crystalline environments (for instance, CN7 and CN6 centers). Nonexponential decays with similar decay times have also been found for the $^1D_2 \rightarrow ^3H_4$ praseodymium transitions in YAG crystals doped with low concentrations of Pr^{3+} ions, and attributed to slightly distorted centers.[27] Results presented in the following sections will show that the $^1D_2$ decay is related to two types of centers. If two centers are involved in the luminescence decay of the $^1D_2$ level, they should also be responsible for the decay of the $^3P_0$ level. Thus, two exponential lifetimes should be resolved in the luminescence decay of the $^3P_0$ level. Experimentally, only one lifetime $\tau \approx 6$ μs is observed, indicating either that both lifetimes are very close and are difficult to resolve or that the concentration of the centers responsible for the unobserved component is low, as is the case for the $^1D_2$ emission. The low-intensity intrinsic luminescence, which overlaps with the tail of the $^3P_0$ emission, also masks the second lifetime component.

D. Pr^{3+} ion concentration

In order to obtain additional information on the luminescence parameters, we have studied the effect of increasing the concentration of Pr^{3+} in the samples. The emission spectra for highly doped samples (1.7×10^{20} cm^{-3}) are mainly the same as those with lower concentration but with several differences which must be related to the redistribution of centers. The most noticeable difference is that the relative intensity of the emissions starting from the $^3P_0$ level is larger in the sample with a higher Pr^{3+} concentration. A similar effect was previously observed in Pr^{3+}-doped La_2O_3,[24] $La_2P_5O_{14}$,[28] and $LiNbO_3$,[29] and attributed to a strong concentration quenching of the $^1D_2$ luminescence due to cross relaxation between Pr^{3+} ions. The $[^1D_2, ^3H_4] \rightarrow [^1G_4, ^3F_{3,4}]$ cross relaxation channel is more efficient than the $[^3P_0, ^3H_4] \rightarrow [^1G_4, ^1G_4]$ channel because the energy mismatch between the levels involved in the latter process is much larger than for the former.[28]

Lifetime measurements show a nonexponential decay for transitions from both $^3P_0$ and $^1D_2$ states. The decay curves are also temperature dependent, indicating that the luminescence process is very complex. Disregarding the small contribution of the minority centers, low-temperature decay curves (see Fig. 7) can be accurately fitted by the continuous Inokuti-Hirayama model:[30]

$$I(t) = I(0)\exp\left[-\frac{t}{\tau_r} - \Gamma\left(1-\frac{3}{s}\right)\frac{N}{C_0}\left(\frac{t}{\tau_r}\right)^{3/s}\right], \qquad (1)$$

where τ_r is the radiative lifetime, N is the concentration of the luminescence centers, $C_0 = 3/4\pi R_0^3$ is the critical concentration, and R_0 is the critical radius defined as the distance at which an isolated donor-acceptor pair has the same transfer rate as the spontaneous decay rate of the donor. The character of the multipolar interaction responsible for the energy transfer process is given by s=6,8,10, . . . for dipole-dipole, dipole-quadrupole, . . . , respectively. The fit shows that the dipole-dipole interaction (s = 6) is the main process responsible for the shortening of the fluorescence lifetimes in samples with a high praseodymium concentration, and yields a value of N/C_0 = 0.91 for the critical ratio. This value

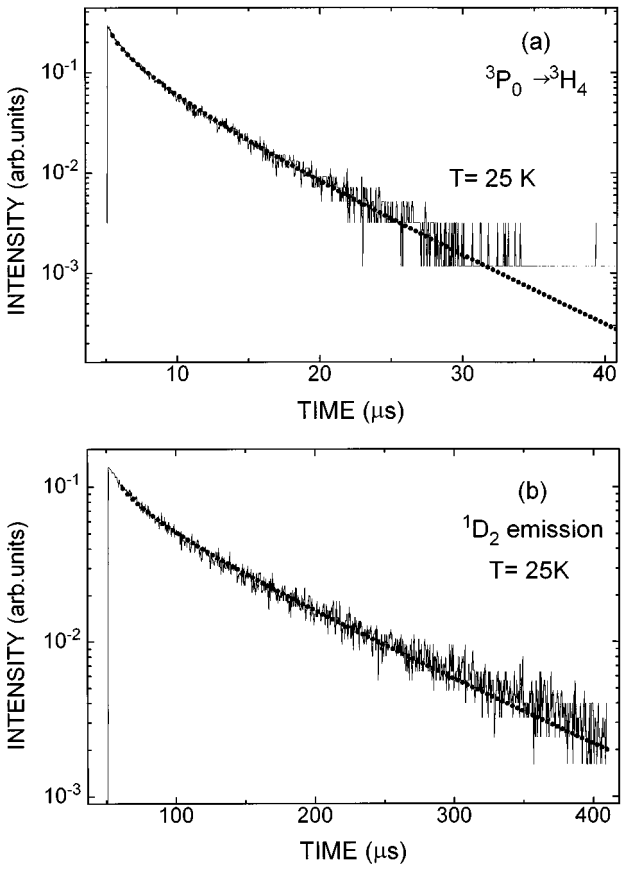

FIG. 7. Decay time curves at 25 K of a praseodymium heavily doped YSZ crystal (a) $^3P_0 \rightarrow ^3H_4$ luminescence and (b) $^1D_2(1) \rightarrow ^3H_4$ luminescence. $\lambda_{ex}=457$ nm. The theoretical fit using the Inokuti-Hirayama model is also shown.

indicates that the concentration of Pr^{3+} ions is close to that necessary to have equal probability for $Pr^{3+} \rightarrow Pr^{3+}$ transfer or radiative decays. From these results, we conclude that energy transfer among Pr^{3+} ions is the mechanism responsible for both the shortening of the fluorescence decay and the intensity decrease of the emission from both levels in heavily doped samples. The accuracy of the fit suggests a statistical distribution of Pr^{3+} ions with the dipole-dipole interaction as the main process responsible for the quenching effect.

From the N/C_0 value, the critical radius R_0 is obtained as a function of the average Pr-Pr distance $R_{ave}=(4\pi N/3)^{-1/3}$. The resulting values are $R_0 \approx R_{ave}$ and $R_0 \approx R_{ave}/2$ for heavily doped and low-doped crystals, respectively. Thus, the complex behavior of the $^1D_2$ decay curves for the samples with a low praseodymium concentration cannot be related to energy transfer processes induced by a concentration effect unless the Pr^{3+} ions are inhomogeneously distributed. The observation of two lifetimes in the $^1D_2$ decay curves in low-doped samples is explained considering Pr^{3+} ions located in sites with different oxygen environments.

E. Judd-Ofelt calculations

The Judd-Ofelt (JO) theory is widely used to calculate $4f$ transition intensities of rare-earth ions in various matrices. Although application of the standard theory to the luminescence of Pr^{3+} ions suffers from several problems,[31] we found the theory could usefully be applied to analyze the luminescence of the Pr^{3+} in YSZ crystals.

The JO theory assumes that the different stark levels in the ground state are equally populated. Due to the strong splitting ($\sim$ 1200 cm^{-1}) of the $^3H_4$ ground state, determined by emission measurements, we have recorded the absorption spectra at moderately high temperatures (500 K) to satisfy as closely as possible the equipopulation requirement. From these spectra the experimental oscillator strengths were determined using the expression

$$f_{expt}=\frac{emc}{\alpha h N \bar{\lambda}}\int \alpha(\lambda)d\lambda, \tag{2}$$

where m is the electron mass, c the speed of light, h Planck's constant, α the fine structure constant, $\bar{\lambda}$ the average transition wavelength, $\alpha(\lambda)$ the absorption coefficient, and N the density of the absorbing ions.

In this theory, the electric dipole oscillator strength between two states characterized by J and J' is given by

$$f_{ED}=\frac{8\pi mc\sigma}{3h(2J+1)}\chi\sum_{t=2,4,6}\Omega_t|\langle J||U^{(t)}||J'\rangle|^2, \tag{3}$$

where σ is the transition wave number, $(2J+1)$ the ground-state degeneracy, and χ the field correction factor $\chi=(n^2+2)^2/9n$, where n is the refractive index of the material.

The concentration of absorbing centers used in the determination of the experimental oscillator strengths must be carefully chosen because only the fraction of praseodymium ions contributing to the optical bands must be taken into account. Two facts must be considered: (1) As was previously mentioned, praseodymium ions could be incorporated not only in the trivalent state but also as Pr^{4+} ions, and (2) praseodymium ions in CN8 (O_h), CN7 (C_{3v}), and CN6 (C_2 or C_{3i}/S_6) environments with very different local symmetries could be present. Charge balance and ionic size arguments suggest that octacoordinated praseodymium ions would prefer the 4+ valence state. The Pr^{4+} ion easily compensates the local oxygen charge and its smaller ionic radius (0.92 Å) is close to those of the Y^{3+} (0.93 Å) and Zr^{4+} (0.80 Å) ions. Pr^{4+} absorption bands were not clearly observed because their expected location is inside the crystal absorption edge. The contribution to the absorption band of Pr^{3+} ions in nearly centrosymmetric sites [CN8 (O_h) and CN6 (C_{3i}/S_6)] can also be disregarded, due to their very low oscillator strength compared with the noncentrosymmetric ones [CN7 (C_{3v}) and CN6 (C_2)]. As a first approximation we will assume that only Pr^{3+} ions in noncentrosymmetric sites contribute to optical bands. The percentage of these centers can be estimated assuming that oxygen vacancies are statistically distributed in the crystal. The probability that one of the Pr ions will have two, one, or zero (Pr^{3+} or Pr^{4+} in nearly centrosymmetric sites) oxygen vacancies as the nearest neighbors can be determined using the expression

$$P(n)=\binom{M}{n}x^n(1-x)^{M-n}, \tag{4}$$

TABLE I. Experimental and calculated oscillator strengths and Judd-Ofelt intensity parameters for Pr^{3+} in YSZ single crystals. Previously reported intensity parameters for Pr^{3+} in other disordered systems are also included.

Transition		Oscillator strength ($\times 10^{-6}$) Expt.	Calc.
$^3H_4\rightarrow$	$^3P_2$	18.70	–
	$^3P_1+^1I_6$	8.36	8.37
	$^3P_0$	6.17	6.15
	$^1D_2$	1.57	1.20
	$^1G_4$	0.29	0.18
	$^3F_3+^3F_4$	12.02	12.06
	$^3F_2$	4.83	4.82
rms		0.13×10^{-6}	

Matrix	JO parameter ($\times 10^{-20}$ cm^2) Ω_2	Ω_4	Ω_6	Reference
ZBLA glass	0.24	4.5	5.4	33
$Na_2O.2B_2O_3$	0.77	4.13	3.07	34
$Li_2O.2B_2O_3$	0.77	3.84	3.58	34
YSZ16	0.34	7.25	3.56	This Work

where $M=8$ is the number of equivalent sites surrounding the praseodymium ion, n is the vacancy number (0,1,2), and x is the total oxygen vacancy fraction (1/20). The resulting values are 0.05, 0.28, and 0.66 for two, one, or zero vacancies, respectively. Thus, we roughly estimate that only ~40% of the praseodymium ions contribute to the optical spectra, with contributions of ≈15% and ≈85% from CN6 and CN7 centers, respectively. These values are in excellent agreement with those previously determined from lifetime measurements. The estimated ~40% implies that a concentration value of $N=10^{19}$ ions/cm^3 must be used to calculate the experimental oscillator strengths in our low-doped crystals.

Matrix elements $|\langle J||U^{(t)}||J'\rangle|^2$ are evaluated in the intermediate-coupling approach using previously reported data.[32] With these values, the Ω_t parameters are calculated from the experimental oscillator strengths and the average value of the energy level positions through a standard least squares fit. We excluded the value of the hypersensitive transition to the $^3P_2$ state as is often done. Results are presented in Table I. For comparison, results obtained for this ion in some disordered systems have also been included.

Once the intensity parameters have been determined, the electric dipole radiative probabilities can be estimated by

$$A_{J\rightarrow J'}=\frac{64\pi^4 e^2}{3h(2J+1)}n^2\chi\sum_{t=2,4,6}\Omega_t|\langle J||U^{(t)}||J'\rangle|^2. \quad (5)$$

Additionally, the radiative lifetimes $\tau_r=1/\Sigma_J A_{J\rightarrow J'}$ and the branching ratios $\beta_{J\rightarrow J'}=A_{J\rightarrow J'}/\Sigma_J A_{J\rightarrow J'}$ can be estimated for the main emission channels.

The calculated radiative lifetimes and branching ratios are shown in Table II together with the experimental values and

TABLE II. Experimental and calculated branching ratios, radiative lifetimes, and quantum efficiencies for Pr^{3+} in YSZ single crystals.

Transition		Branching Ratios Expt.	Calc.
$^3P_0\rightarrow$	$^1D_2$		1×10^{-5}
	$^1G_4$	—	0.027
	$^3F_3+^3F_4$	0.024	0.143
	$^3F_2$	0.095	0.023
	$^3H_6$	—	0.076
	$^3H_5$	0.218	0
	$^3H_4$	0.663	0.731
$^1D_2\rightarrow$	$^1G_4$		0.064
	$^3F_3+^3F_4$	0.130	0.084
	$^3F_2$	0.217	0.229
	$^3H_6$	0.216	0.247
	$^3H_5$	0.062	0.011
	$^3H_4$	0.366	0.363

	Lifetimes (μs) τ_r	τ_{expt}(RT)	τ_{expt}(LHeT)
$^3P_2$	9.5		
$^1I_6$	40.0		
$^3P_1$	9.0		
$^3P_0$	8.6	1.8	6.1
$^1D_2$	186	180	180
$^1G_4$	960		

	Quantum efficiencies η(RT)	η(LHeT)
$^3P_0$	0.21	0.70
$^1D_2$	0.97	0.97

quantum efficiencies. Transitions originating in the $^3P_0$ level which appear in the emission spectrum agree with the calculated maximum branching ratios. The poor agreement of the $^3P_0$ branching ratios is caused by the high-experimental uncertainty, due to overlapping of the high intensity $^1D_2$ emission bands. Moreover, the branching ratio values of the $^3P_0\rightarrow{}^3H_5$ emissions (well resolved in the emission spectra) are strongly affected by the $\Omega_5|\langle J||U^{(5)}||J'\rangle|^2$ product which is not taken into account in this calculation.[35]

The agreement is better for the transitions which originate from the $^1D_2$ state. The data shown in Table II also indicate that a radiative occupancy of the $^1D_2$ level from the $^3P_0$ level is not likely to occur. In contrast, the $^1G_4$ level can be populated via $^3P_0$ and $^1D_2$ radiative transitions. This would explain the appearance of transitions starting at the $^1G_4$ state in the emission spectra. Due to the large energy separation of this state from the $^3P_0$ and $^1D_2$ ones, population of the $^1G_4$ state via multiphonon relaxation processes is not expected. Last, cross relaxation within pairs of Pr^{3+} ions could populate the $^1G_4$ state via the $[^3P_0,{}^3H_4]\rightarrow[^1G_4,{}^3H_6]$ re-

laxation scheme. However, this process was shown to occur via an exchange interaction which is effective only for very short distances.[36]

Theoretical and experimental lifetime values are in good agreement and provide quantum efficiency values of 0.2 for the $^3P_0$ level and ~ 1 for the $^1D_2$ state at room temperature. In the absence of energy transfer processes (low-doped samples), a value close to unity for the quantum efficiency of the $^1D_2$ luminescence appears to be reasonable because multiphonon relaxation processes to the distant $^1G_4$ state are unlikely. This value suggests that the only channel for the $^1D_2$ depopulation is the radiative relaxation. Moreover, assuming that a decrease of the radiative efficiency of the $^3P_0$ level implies an increase in the population of the $^1D_2$ level, as the excitation spectrum indicates, the quantum efficiency of the $^3P_0$ level roughly coincides with the fraction of the $^3P_0$-integrated absorption intensity that is not present in the excitation spectrum of the $^1D_2$ luminescence. The experimental resulting value for the room-temperature quantum efficiency of the $^3P_0$ level is $\eta(^3P_0) \approx 0.2$–0.3, which is also in good agreement with the value predicted by the JO calculations.

F. Fluorescence dynamics

Thermally assisted relaxation from the $^3P_0$ to the $^1D_2$ levels appears to be the mechanism responsible for the luminescence observations in low-doped samples. The evidence is (1) the presence of the $^3P_J + ^1I_6$ states in the excitation spectra of the $^1D_2$ luminescence, (2) both the exponential decay curves of the $^3P_0$ emissions and their temperature dependence, and (3) the increase of the $^3P_0$ intensities as the temperature decreases. The first nonradiative channel to be considered is the $^3P_0$ to $^1D_2$ multiphonon relaxation. The average energy gap between these two levels is ~ 3400 cm^{-1} and the highest frequency of the lattice phonons in YSZ is 685 cm^{-1};[37] hence, at least five phonons are necessary in this process. Assuming that only phonons with the highest frequency are involved, a multiphonon relaxation rate of $W_{\mathrm{NR}}(0) \approx 10^3$ s^{-1} is calculated using the Van Dijk–Shuurmans modified gap law[38,39]

$$W_{\mathrm{NR}}(0) = 10^7 \exp[-4.5\times 10^{-3}(\Delta E - 2\hbar\omega)]. \qquad (6)$$

A value of 10^3–10^4 s^{-1} for the $W_{\mathrm{NR}}(0)$ relaxation rate indicates that the $^3P_0$ luminescence lifetime should decrease slightly as the temperature increases, in contrast with our experimental findings. In this calculation we have arbitrarily chosen the highest phonon frequency for the multiphonon relaxation, even though the electron-phonon coupling may occasionally be so weak that the effective phonon frequency could be significantly lower.[40] Actually, in Er^{+3}-doped YSZ, a phonon frequency of 520 cm^{-1} has been reported for the phonons involved in the multiphonon relaxation.[12] With this phonon frequency, seven phonons are needed to fill up the energy gap between the $^3P_0$ and $^1D_2$ levels. A multiphonon relaxation process involving the generation of seven phonons is much less likely to occur according to the Moss-Weber dependence of the nonradiative relaxation rate on the number of effective phonons.[39]

Another possible channel responsible for the deexcitation to the $^1D_2$ is the well-known relaxation via the $4f5d$ level.

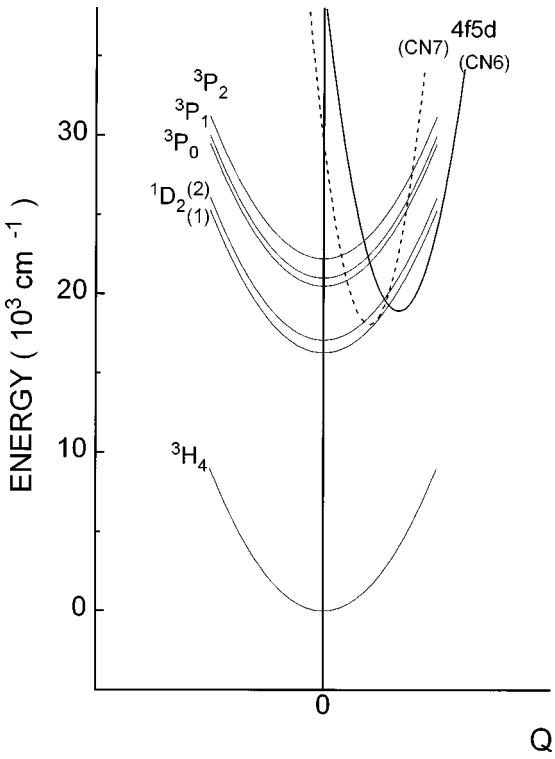

FIG. 8. Configurational coordinate model for YSZ:Pr^{3+}.

Direct $4f5d$ to $4f^2$ relaxation has been observed in YAG crystals and has been invoked as the process also operating in other oxides.[22–25,41] We have already mentioned the appearance of a band in the UV region of the excitation spectrum, and have assigned this band to the $4f5d$ excited configuration of the Pr^{3+} ions. Moreover, the high intensity of the $^1D_2$ emission under UV excitation must be related to the direct feeding of this level via the $4f5d$ relaxation. We will use this approach as a plausible explanation for the previously described luminescence dependence on the temperature.

A tentative configurational coordinate model is displayed in Fig. 8. The diagram was drawn based on the spectral positions of the $^3P_{0,1,2} \rightarrow {}^3H_4$ and $^1D_2 \rightarrow {}^3H_4$ transitions and the edge of the $4f5d$ excitation bands. The two $4f5d$ parabolas are associated, respectively, with the two main luminescence centers CN7 and CN6. The position and force constant of the low-lying $4f5d$ excited state have been carefully analyzed by de Mello Donegá *et al.*[25] in several oxides. The position of the $4f5d$ edge in the excitation spectrum is very sensitive to the crystal field intensity, and is related primarily to the Pr-O distance, shifting to lower energies with larger crystal field intensities. Due to the overlapping between the oxygen and the $4f5d$ Pr^{3+} wave functions, the interconfigurational band has some charge transfer character. Under this hypothesis, oxygen vacancies near Pr^{3+} ions would decrease the overlap between the $4f5d$ wave functions of the Pr^{3+} ion and those of the O^{2-} ligands, resulting in a higher-energy shift in the $4f5d$ excitation band. Thus, we have assigned the $4f5d$ parabola with low Q to CN7 centers and that with high Q to CN6 centers. The main difference is the energy gap between the $^3P_0$ and the $4f5d$ crossover. For CN6 centers, this energy gap is moderately large ($\sim$ 1500 cm^{-1}) and thermal populations of the $^3P_1$ and $^3P_2$ levels

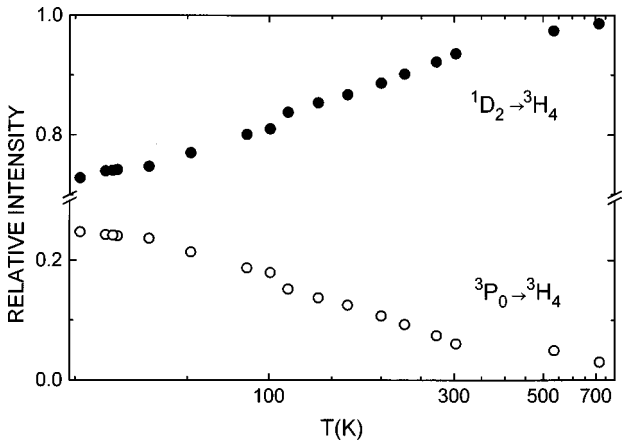

FIG. 9. Temperature dependence of the emission relative intensity for the $^3P_0$ and $^1D_2$ emission levels.

are attended by an emission loss of the $^3P_0$ level. Thermal population also makes it possible for the electrons to reach the crossover between the $^3P_{1,2}$ states and the $4f5d$ configuration and to relax down to the $^1D_2$ level via the $4f5d$ configuration. In contrast, for CN7 centers the gap is very small ($\sim$120–170 cm^{-1}), and thermal population of the $^3P_{1,2}$ states is not possible. The very efficient quenching of the $^3P_0$ luminescence is attended by the population of the $^1D_2$ state via the $4f5d$ crossover.

To verify the configurational coordinate model we have analyzed the temperature dependence of the emission intensity. Figure 9 shows the temperature dependence for low-doped samples of the relative intensity (determined by dividing the integrated emission intensity of each transition band by the total integrated intensity) for transitions from the $^1D_2$ and $^3P_0$ states under excitation in the $^3P_2$ absorption region (457 nm). This plot clearly shows that raising the temperature increases the number of photons emitted by the $^1D_2$ state and decreases the number of those emitted by the $^3P_0$ states. Figure 10 displays the temperature dependence of the relative intensity of the $^3P_0 \rightarrow {}^3H_4$, $^3P_1 \rightarrow {}^3H_5$ and $^1D_2(2) \rightarrow {}^3H_4$ transitions in low-doped samples. The last two transitions start at thermally populated levels. The intensity of the $^3P_0 \rightarrow {}^3H_4$ transition continuously decreases as temperature increases, whereas for the $^1D_2(2) \rightarrow {}^3H_4$ transition it continuously increases with temperature. The emission intensity from the $^3P_1$ states exhibits a more complicated behavior: It rises up to $\sim$300 K and decreases slightly for higher temperatures.

The model we shall consider is shown schematically in Fig. 11. The energy levels correspond to the ^3P_J multiplet and the $4f5d$ crossover parabolas depicted in Fig. 8. The latter levels are located at different positions for CN6 and CN7 centers and act as luminescence traps. Since both CN6 and CN7 centers contribute to the $^3P_0$ emission band, the temperature dependence of the $^3P_0$ intensity can be given by Mott's formula adding the contributions of the two centers:

$$I(T) = I^{\mathrm{CN6}}_{^3P_0}(T) + I^{\mathrm{CN7}}_{^3P_0}(T), \tag{7}$$

where

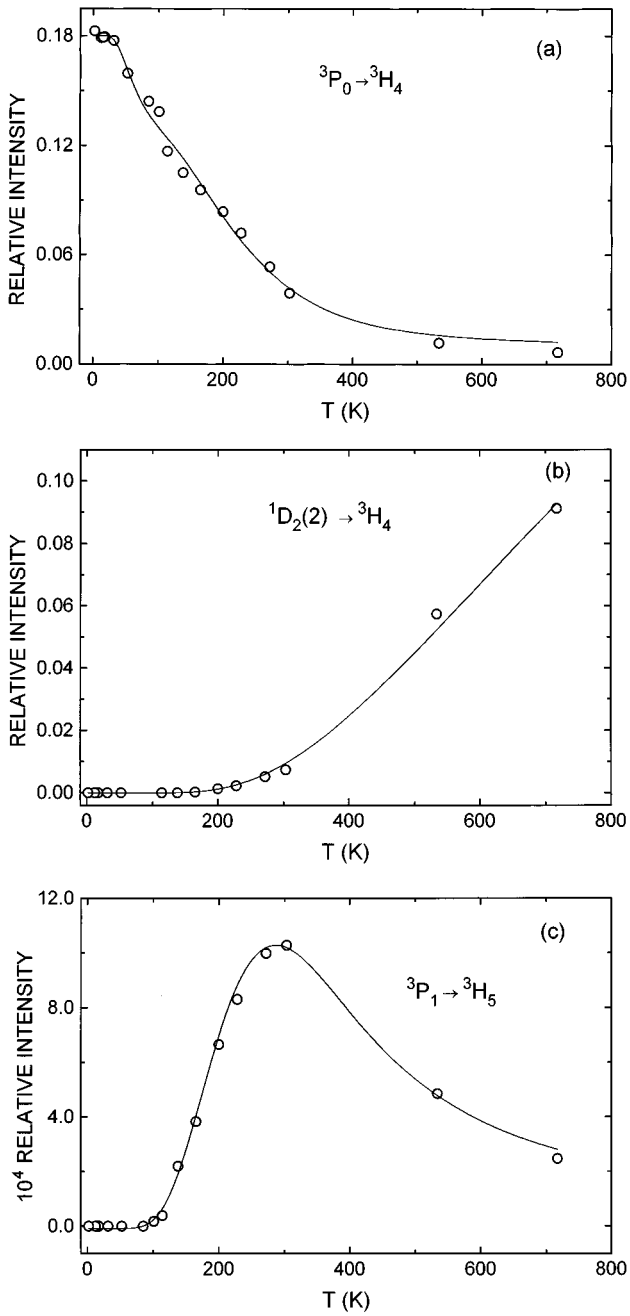

FIG. 10. Relative emission intensity vs temperature for (a) $^3P_0 \rightarrow {}^3H_4$ transition, (b) $^1D_2(2) \rightarrow {}^3H_4$ transition, and (c) $^3P_1 \rightarrow {}^3H_5$ transition. The solid lines represent the corresponding theoretical fit.

$$I^{\mathrm{CN6}}_{^3P_0}(T) = \frac{I^{\mathrm{CN6}}_{^3P_0}(0)}{1 + A\exp(-E_{01}/kT) + B\exp(-E_{02}/kT)} \tag{8}$$

and

$$I^{\mathrm{CN7}}_{^3P_0}(T) = \frac{I^{\mathrm{CN7}}_{^3P_0}(0)}{1 + C\exp(-E_T/kT)} \tag{9}$$

describe the contribution of each center. In the previous expressions A, B, and C are adjustable parameters, $I^{\mathrm{CN6}}(0)$ and $I^{\mathrm{CN7}}(0)$ are the intensities at $T=0$, and E_{01}, E_{02}, and E_T are

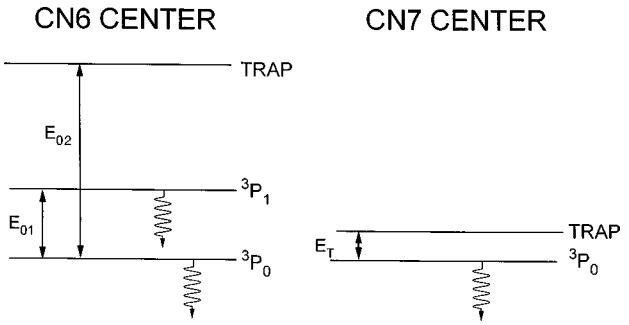

FIG. 11. Eschematic energy-level diagram for CN6 and CN7 centers.

the energy-level separations for the two centers (see Fig. 11). The result of the calculation is depicted in Fig. 10(a). The resulting activation energies are $E_T = 120\ \mathrm{cm}^{-1}$ and $E_{02} = 1440\ \mathrm{cm}^{-1}$. The $E_{01} = 500\ \mathrm{cm}^{-1}$ coincides with the experimental ($516\ \mathrm{cm}^{-1}$) energy separation between $^3P_0$ and $^3P_1$ states. An activation energy of $120\ \mathrm{cm}^{-1}$ implies that at very low temperatures ($T \sim 2$ K), the direct $^3P_0 \rightarrow {}^3H_4$ relaxation should be strong. However, the large inhomogenous broadened halfwidth of the $^3P_0$ absorption band makes the $^3P_0$ to $^1D_2$ relaxation via the $4f5d$ crossover also possible.

In order to obtain additional information, the temperature dependence of the reciprocal of the $^3P_0$ lifetime (displayed in Fig. 12) was also analyzed with our configurational coordinate model for low-doped samples. The temperature dependence of the $^3P_0$ decay time can be described by[39]

$$\frac{1}{\tau} = \frac{1}{\tau_r} + W_{\mathrm{NR}}(0)\exp(-\Delta E_Q/kT), \tag{10}$$

where $W_{\mathrm{NR}}(0)$ is the nonradiative relaxation rate and ΔE_Q the activation energy. The fit depicted in Fig. 12 yields an activation energy of $170\ \mathrm{cm}^{-1}$ and a nonradiative relaxation rate of $\sim 10^6\ \mathrm{s}^{-1}$. This result agrees with the activation energy for CN7 centers determined from intensity measurements [see Fig. 11(a)]. Since the depopulation channel $4f5d$ for CN6 centers starts at an energy much higher than for CN7 centers, the expected lifetime value for CN6 centers must be longer than for CN7 centers: $\tau_{\mathrm{CN6}} > \tau_{\mathrm{CN7}}$. Thermal population of the $^3P_1$ level implies that the CN6 lifetime

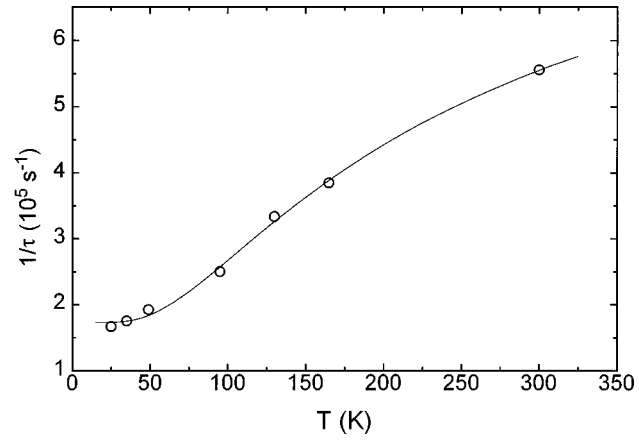

FIG. 12. Reciprocal of the lifetime of the $^3P_0$ level as a function of temperature. Solid line is a plot of the theoretical fit.

decreases with temperature. Unfortunately, the CN6 contribution is not clearly established from the experimental results. The relatively low number of CN6 centers (15%) and the presence of the intrinsic luminescence, responsible for the previously mentioned long-lived background in the lifetime measurements, complicates the experimental determination of the two expected lifetime components.

In accordance with our model, the $^3P_1$ levels are only populated for the CN6 center. Assuming that both $^3P_1$ and $^1D_2(2)$ levels are thermally populated from $^3P_0$ and $^1D_2(1)$ levels, respectively, the temperature dependence of their intensities is described by

$$I_{^1D_2(2)}(T) = \frac{I_{^1D_2(1)}(0)G\exp(-\Delta E/kT)}{1 + D\exp(-\Delta E/kT)} \tag{11}$$

and

$$I^{\mathrm{CN6}}_{^3P_1}(T) = \frac{I^{\mathrm{CN6}}_{^3P_0}(T)F\exp(-E_{01}/kT) + I^{\mathrm{CN6}}_{^3P_1}(0)}{1 + H\exp[-(E_{02}-E_{01})/kT]}, \tag{12}$$

where D, F, G, and H are adjustable parameters, $I_{^1D_2(1)}(0)$ and $I^{\mathrm{CN6}}_{^3P_1}(0)$ are the intensities at $T=0$ for both levels, and ΔE is the energy separation between $^1D_2(1)$ and $^1D_2(2)$ levels. With the previously obtained values for E_{01} and E_{02}, and the experimental value $\Delta E = 833\ \mathrm{cm}^{-1}$, the temperature dependence of the luminescence intensities of the $^3P_1$ and $^1D_2(2)$ states is reproduced using Eqs. (11) and (12). The resulting fitting curves are depicted in Figs. 10(b) and 10(c). The agreement with the experimental results is excellent and validates the proposed model.

The activation energy ($1440\ \mathrm{cm}^{-1}$) determined for the luminescence trap of the CN6 center is close to the energy position of the $^3P_2$ state (located at $\sim 1900\ \mathrm{cm}^{-1}$ above the $^3P_0$ level), indicating that the energy trap position roughly coincides with the presumable energy position of the $4f5d$ crossover.

Last, nonradiative $^3P_0$ relaxation via host lattice excited states can occur provided that the lattice states are at the right energies. In this case, however, the excitation energy appears to be mostly lost via nonradiative channels or by intrinsic luminescence rather than to populate the $^1D_2$ level which is primarily responsible for the Pr^{3+} luminescence.

IV. CONCLUSIONS

Optical absorption and luminescence of Pr^{3+}-doped YSZ crystals have been analyzed. The dynamics of the Pr^{3+} luminescence in YSZ is satisfactorily explained assuming that Pr^{3+} ions are present in two oxygen coordinations (assigned to CN7 and CN6 centers) with a statistical distribution. The energy position of the excited $4f5d$ configuration plays an important role in the fluorescence dynamics. The $^3P_0$-$4f5d$ crossover energy gap is very different for each center: ~ 120–$170\ \mathrm{cm}^{-1}$ and $\sim 1500\ \mathrm{cm}^{-1}$ for the CN7 and CN6 centers, respectively. For the minority CN6 centers, thermal population of the $^3P_{1,2}$ levels is attended by an emission loss of the $^3P_0$ level, which eventually relaxes down to the $^1D_2$ level via the $4f5d$ configuration. In contrast, for the majority CN7 centers, excitation in the $^3P_{0,1,2}$ region rapidly

relaxes (via the $4f5d$ crossover) to the $^1D_2$ states from which the luminescence primarily takes place. The fluorescence emission starting at the $^1D_2$ state exhibits a complex decay with lifetimes of 180 μs and 53 μs, due to contributions of CN7 and CN6 centers, respectively. For the $^3P_0$ emission, the contribution of the minority centers was not resolved. This decay is nearly exponential with a lifetime of ~ 6 μs at low temperatures which strongly decreases as the temperature is raised. Under the assumption that only noncentrosymmetric praseodymium ions ($\sim 40\%$ of the total concentration) contribute to the luminescence emission, the Judd-Ofelt theory is used to estimate the quantum efficiencies of the main luminescence channels. A quantum efficiency of 0.2 is obtained for the $^3P_0$ emission at RT. This value increases to 0.7 at low temperature. The estimated value for the quantum efficiency of the $^1D_2$ state is close to 1.

Energy transfer has been observed in heavily doped samples and is related to cross relaxation processes among the nearest Pr^{3+} ions. Decay curves were analyzed using the Inokuti-Hirayama model and indicated that dipole-dipole interaction is responsible for the quenching effect of both lifetime and emission intensity.

ACKNOWLEDGMENTS

This work has been supported by the Comisión Asesora de Investigación Científica y Técnica of the Spanish Government and the Comunidad Autónoma de Madrid (CAM). We are indebted to J. García Solé for his critical reading of the manuscript and for his assistance in the lifetime measurements at the Universidad Autónoma de Madrid (UAM). The help of J.M. Calleja (UAM) with the measurements below 15 K is also acknowledged.

[1] A. A. Kaminskii, *Laser Crystals*, Springer Series in Optical Sciences, Vol. 14 (Springer-Verlag, Berlin, 1981).
[2] A. A. Kaminskii, Ann. Phys. (Paris) **16**, 639 (1991).
[3] R. G. Smart, J. N. Carter, A. C. Tropper, D. C. Hanna, S. T. Davey, S. F. Carter, and D. Szebesta, Opt. Commun. **86**, 337 (1991).
[4] R. G. Smart, D. C. Hanna, A. C. Tropper, S. T. Davey, S. F. Carter, and D. Szebesta, Electron. Lett. **127**, 1307 (1991).
[5] J. Y. Allain, M. Monerie, and H. Poignant, Electron. Lett. **27**, 189 (1991).
[6] A. A. Ballman, S. P. S. Porto, and A. Yariv, J. Appl. Phys. **34**, 3155 (1963).
[7] See, for example, *Science and Technology of Zirconia*, edited by A. H. Heure and L. W. Hobbs, Ser. Adv. Ceramics, Vol. 3 (American Ceramic Society, Columbus, OH, 1981).
[8] J. Dexper-Ghys, M. Faucher, and P. Caro, J. Solid State Chem. **54**, 179 (1984).
[9] M. H. Tuilier, J. Dexper-Ghys, H. Dexpert, and P. Lagarde, J. Solid State Chem. **69**, 153 (1987).
[10] Ping Li, I-Wei Chen, and J. E. Penner-Hahn, Phys. Rev. B **48**, 10 074 (1993).
[11] H. Yugami, A. Koike, M. Ishigame, and T. Suemoto, Phys. Rev. B **44**, 9214 (1991).
[12] R. I. Merino, V. M. Orera, R. Cases, and M. A. Chamarro, J. Phys.: Condens. Matter **3**, 8491 (1991).
[13] R. I. Merino and V. M. Orera, Solid State Commun. **88**, 435 (1993).
[14] H. Arashi, Phys. Status Solidi A **10**, 107 (1972).
[15] A. F. Wells, *Structural Inorganic Chemistry*, 5nd ed. (Claredon Press, Oxford, 1984).
[16] T. H. Etsell and S. N. Flengas, Chem. Rev. **70**, 339 (1970).
[17] M. Kunz, H. Kretschmann, W. Assmuss, and C. Klingshirn, J. Lumin. **37**, 123 (1987).
[18] G. H. Dieke, *Spectra and Energy Levels of Rare Earth Ions in Crystals* (Wiley Interscience, New York, 1968).
[19] V. M. Orera, R. I. Merino, Y. Chen, R. Cases, and P. J. Alonso, Phys. Rev. B **42**, 9782 (1990).
[20] S. E. Paje and J. Llopis, Appl. Phys. A **57**, 225 (1993).
[21] B. Savoini, J. E. Muñoz Santiuste, R. González, and Y. Chen, J. Lumin. **72-74**, 714 (1997).
[22] H. E. Hoefdraad and G. Blasse, Phys. Status Solidi A **29**, K95 (1975).
[23] G. C. Aumüller, W. Köstler, B. C. Grabmaier, and R. Frey, J. Phys. Chem. Solids **55**, 767 (1994).
[24] C. de Mello Donegá, A. Ellens, A. Meijerink, and G. Blasse, J. Phys. Chem. Solids **54**, 293 (1993).
[25] C. de Mello Donegá, A. Meijerink, and G. Blasse, J. Phys. Chem. Solids **56**, 673 (1995).
[26] S. E. Paje and J. Llopis, Appl. Phys. A **59**, 569 (1994).
[27] M. Malinowski, P. Szczepanski, W. Wolinski, R. Wolski, and Z. Frukacz, J. Phys.: Condens. Matter **5**, 6469 (1993).
[28] H. Dornauf and J. Heber, J. Lumin. **22**, 1 (1980).
[29] A. Lorenzo, L. E. Bausá, and J. García Solé, Phys. Rev. B **51**, 16 643 (1995).
[30] M. Inokuti and F. Hirayama, J. Chem. Phys. **43**, 1978 (1965).
[31] Different attempts to modify the JO theory have recently been made in order to standardize the method used to fit the Pr^{3+} absorption bands. See, for example, P. Goldner and F. Auzel, J. Appl. Phys. **79**, 7972 (1996) and other references cited therein.
[32] M. J. Weber, J. Chem. Phys. **48**, 4774 (1968).
[33] M. Eyal, E. Greenberg, R. Reisfeld, and M. Spector, Chem. Phys. Lett. **117**, 108 (1985).
[34] J. Hormadaly and R. Reisfeld, J. Non-Cryst. Solids **30**, 337 (1979).
[35] R. D. Peacock, Struct. Bond. **22**, 83 (1975).
[36] J. C. Vial and R. Buisson, J. Phys. (France) Lett. **43**, L-745 (1982).
[37] V. A. Aleksandrov, A. V. Vasilev, Yu. A. Kalgin, L. D. Kislovskii, and V. M. Tatarintsev, Opt. Spectrosc. **40**, 627 (1967).
[38] J. M. F. van Dijk and M. F. H. Schuurmans, J. Chem. Phys. **78**, 5317 (1983).
[39] B. Henderson and G. F. Imbusch, *Optical Spectroscopy of Inorganic Solids* (Clarendon Press, Oxford, 1989).
[40] L. A. Riseberg and M. J. Weber, in *Relaxation Phenomena in Rare Earth Luminescence*, Progress in Optics XIV, edited by E. Wolf (North-Holland, Amsterdam, 1976).
[41] G. Blasse, *Luminescence of Inorganic Solids*, edited by B. DiBartolo (Plenum Press, New York, 1978).